

Group 2

Full Name	Student ID
Adam Misa	2208512
Artemis Angeloupoulou	2192977
Hidis Mottaghi Jahromi	2125587
Henk Gongriep	1980114
Oskar Hovinga	1917757

Tutor : Dr. Nikolay Kosinov

Contents

1	Introduction	1
2	Characterization of Inverse CeO_x/Co catalysts	1
2.1	H ₂ -TPR (Temperature-Programmed Reduction)	1
2.2	CO chemisorption	1
2.3	X-ray diffraction (XRD)	2
2.4	XANES and Ce Oxidation States	2
2.5	Operando Infrared (IR) Spectroscopy	2
2.6	CO ₂ methanation performance	3
3	Conclusion	3
4	References	4
A	Appendix A: Supportive Information	5

1 | Introduction

The increasing atmospheric concentration of CO₂ has driven the need for efficient catalytic technologies to convert CO₂ into valuable chemicals and fuels. Among various routes, CO₂ methanation—the hydrogenation of CO₂ to CH₄—offers a promising pathway for synthetic natural gas production and renewable energy storage. Conventional methanation catalysts often consist of cobalt or nickel dispersed on reducible oxide supports such as CeO₂. In this study, we investigate a series of inverse CeO_x/Co catalysts synthesized via flame-spray pyrolysis (FSP), systematically varying the cerium content (0–20 mol%). These catalysts are compared to conventional Co/CeO_x systems to assess how structural interactions at the oxide–metal interface influence methanation activity and selectivity. Using a combination of characterization techniques, we aim to elucidate the structure–performance relationships and mechanistic differences between the samples and to compare qualitatively to the conventional CoO_x/Ce_x catalytic system.

2 | Characterization of Inverse CeO_x/Co catalysts

2.1 | H₂-TPR (Temperature-Programmed Reduction)

From the H₂-TPR profiles in Fig. 2.1, we observe that the 0Ce100Co sample shows two sharp and intense reduction peaks centered at lower temperatures, around ~280–350 °C. These peaks correspond to the sequential reduction of Co₃O₄ to CoO and then to metallic Co, which is a typical two-step reduction pathway [1]. This behavior suggests that cobalt oxides in the absence of ceria are readily reducible, undergoing rapid reduction with high hydrogen consumption. As ceria content increases, we observe that the reduction peaks shift to higher temperatures and become broader. For instance, in the 20Ce80Co sample, the main reduction peak is delayed and less defined, with a noticeable broad shoulder appearing around 500 °C. This behavior indicates that reduction becomes more difficult with higher ceria loading. Based on the literature by Lin et al. [2], this shift in reduction temperature and broadening of the peaks is attributed to the strong interaction between cobalt species and CeO₂, which forms Co–O–Ce interfacial structures. A reduction feature corresponding to CeO₂ is also observed around 500–600 °C, in agreement with Jan et al. [3]. Furthermore, we observe that the intensity of the hydrogen consumption peaks decreases with increasing ceria content. This suggests a lower degree of reducibility, which is consistent with the findings of Roberge *et al.* [4], which can stabilize the oxide structure due to structural modification and can be observed in Fig 2.1 as well. This behavior of cobalt-based catalysts significantly depends on catalyst architecture, as evidenced by the H₂-TPR profiles. In the study by O’Connell *et al.* [5], indicating easier reducibility of cobalt oxides due to weaker metal support interactions on the catalytic surface. In contrast, in the inverse Ce/Co catalysts studied where ceria is deposited on cobalt oxide the reduction peaks shift to higher temperatures with increasing ceria content. This shift suggests stronger Co–O–Ce interactions on the surface that stabilize cobalt oxide species, making them more stable at higher temperature.

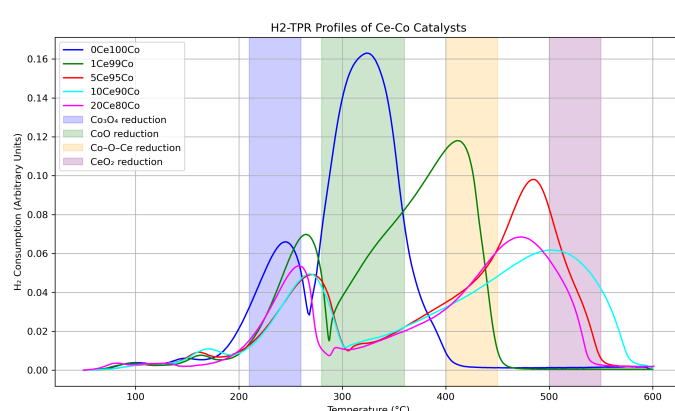


Figure 2.1: H₂-TPR Profiles of Ce-Co Catalysts

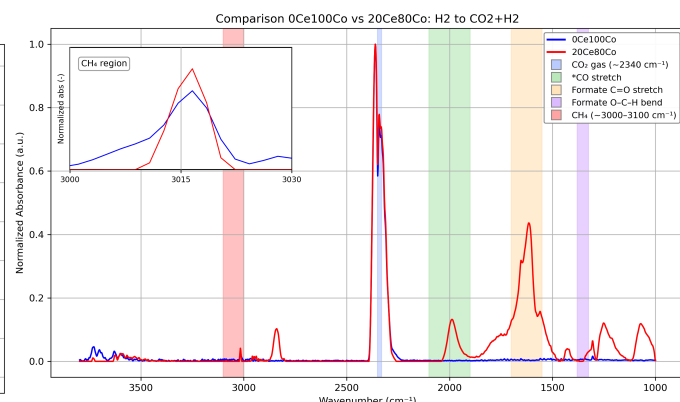


Figure 2.2: Comparison 0Ce100Co vs 20Ce80Co and zoom in CH₄ (in the 3000–3050 cm⁻¹ range)

2.2 | CO chemisorption

Our CO chemisorption results, summarized in Table A.1, demonstrate a clear enhancement in cobalt dispersion and CO uptake with increasing cerium content. The 20Ce80Co sample, which contains the lowest cobalt loading (0.63 wt.%), exhibited the highest dispersion (2.0%) and CO adsorption capacity (0.2088 mmol/g), confirming that cerium plays a significant role in promoting surface accessibility of cobalt. This trend aligns with previous reports by Lin et al. [2], who showed that CeO₂ increases dispersion and enhances catalytic activity. Similarly, Zhou et al. [6] demonstrated that the addition of Ce to Co₃O₄ catalysts improves both dispersion and CO₂ methanation activity through enhanced surface basicity and metal-support interactions. Furthermore, the role of ceria’s oxygen vacancies, as discussed by Campbell and Peden [7], helps rationalize our findings: oxygen vacancies not only stabilize Co particles but also participate

in CO₂ activation by offering reactive Ce³⁺ surface sites. The combined evidence supports the conclusion that our Ce-on-Co catalyst effectively replicates many of the benefits observed in traditional Co-on-CeO₂ supported systems. In their work, the authors attribute the decrease in dispersion with increasing cobalt loading to the formation of larger cobalt domains. This trend was explained by the limited capacity of the ceria surface to accommodate increasing amounts of cobalt, which leads to particle growth and a reduction in accessible active sites. A similar relationship is observed in our Ce-Co system. Although the dispersion values are lower but we observe that decreasing cobalt content still results in higher dispersion. This suggests that cerium incorporation inhibits cobalt aggregation and maintains a greater fraction of surface-accessible Co sites. Thus, our Ce-on-Co catalysts exhibit a structure–dispersion relationship comparable to that of classical Co-on-CeO₂ systems, reinforcing the role of ceria in tuning dispersion, as described by O’Connell *et al.*

2.3 | X-ray diffraction (XRD)

XRD analysis was performed and the miller indices were calculated for all the peaks using the 2θ-values, see Fig. A.13 and Table A.2. With increasing Ce concentration, new diffraction peaks emerge at 28.7° and 47.6° in the 10Ce90Co and 20Ce80Co samples, while they remain absent at lower Ce loadings. This suggests that at lower concentrations, Ce is incorporated into the Co-containing phase without forming a distinct crystalline structure. However, at higher concentrations, a threshold is reached where phase segregation occurs, leading to the formation of a separate Ce-containing phase. The observed peaks correspond to the (111) and (220) reflections of CeO₂, indicating the presence of crystalline ceria in these samples. Oxygen vacancies in CeO₂ have been linked to catalytic activity in Ceria catalyst [8]. The higher performance of the 10Ce90Co and 20Ce80Co samples from the CO₂ methanation performance can be explained by the presence of oxygen vacancies in the new CeO₂ phase. A higher Ce concentration results in broader and less intense XRD peaks, indicating a lower degree of crystallinity. Increased crystallinity can enhance structural stability and lead to more well-defined active sites, which may improve catalyst durability. However, excessive crystallinity can also reduce the number of accessible active sites, limit structural flexibility, and potentially lower catalytic activity. Amorphous materials, on the other hand, tend to have more defects, unsaturated coordination sites, and potentially higher surface areas, which can enhance adsorption and reaction rates.

The crystallite size of cobalt was estimated using Scherrer’s equation. This was based on the largest cobalt diffraction peak at 36.7° which could be attributed to cobalt because it is present in the pure cobalt sample. The calculated particle sizes are reported in Table A.2. The crystal size remains unchanged across different Ce concentrations. Literature suggests that cobalt with a similar crystal size is associated with high catalytic activity [9]. The large peaks at 36.7° 59.5° and 65.2° can be attributed to cobalt because they are present in the pure Cobalt sample. Based on the H₂-TPR and IR results, these peaks are associated with the presence of Co₃O₄ and CoO. The observed reduction in peak intensity is due to the stepwise reduction of Co₃O₄ to CoO, followed by further reduction to metallic Co.

2.4 | XANES and Ce Oxidation States

The XANES L₃ Edge data as shown in Fig. A.14 was used to determine the oxidation state and geometry change of surface atoms for the xCeyCo samples. The white line feature drastically decreases upon an increase in the Ce concentration. Indicating a shift of the dominant oxidation state from Ce³⁺ to Ce⁴⁺ with increasing Ce concentration. The surface geometry changes slightly with the coexistence of the oxidation states of Ce⁺³ and Ce⁺⁴ towards a more dominant Ce⁺⁴ crystal structure in samples with 5, 10, and 20 mol% Ce, without significantly changing the lattice distances. Furthermore, this change can also increase the available number of stored/available oxygen, which can influence the catalytic cycle. [10] This makes cerium a very flexible and stable component in catalyst design for red-ox reaction even at high temperatures [11].

2.5 | Operando Infrared (IR) Spectroscopy

The catalytic performance and reaction mechanisms were investigated using Operando Infrared (IR) Spectroscopy under four defined reaction conditions, as outlined in Fig. A.10. Background-subtracted spectra for both 0Ce100Co and 20Ce80Co are presented and discussed in detail in the Appendix. Both catalysts show immediate methane formation, as indicated by CH₄ vibrational bands (\sim 3000–3100 cm⁻¹) appearing during the first CO₂ pulse. This activity without requiring a highly H₂ environment-suggests that both surfaces are active for low-temperature methanation. However, for 0Ce100Co, CO vibrational bands only emerge under excess CO₂, indicating limited CO formation, which confirms the higher selectivity of CH₄ at 200°C. In contrast, 20Ce80Co exhibits clear CO bands under standard conditions, suggesting more effective CO₂ activation and stabilization of intermediates due to ceria promotion [12]. Moreover, strong formate bands in 20Ce80Co indicate that formates participate in the reaction without inhibiting methane production. Despite its lower CH₄ selectivity, 20Ce80Co shows similar CO₂ adsorption behavior to 0Ce100Co. The normalized IR intensity diagrams were generated using the initial data obtained under the first set of reduction gas to (CO₂) + (H₂). The normalized IR decay behavior observed for 20Ce80Co shown in Figure 2.3 from this figure, we observe that the formation of methane (CH₄) correlates well with the appearance of carbonyl species (CO and formate

C=O). This trend suggests a sequential reaction pathway in which carbon dioxide (CO₂) is first reduced to carbon monoxide (CO), followed by further reduction to methane (CH₄). From Figure 2.4, we observe that the formation of methane (CH₄) correlates more strongly with the presence of formate species (Formate_C=O and Formate_OCH). However, the pathway for methane formation in this case is not clearly identifiable based on our current data. Therefore, we cannot conclusively determine the reaction mechanism for the 0Ce100Co catalyst. In conclusion, the unpromoted Co catalyst (0Ce100Co) shown in Figure 2.4 exhibits rapid CH₄ formation with minimal intermediate accumulation, suggesting a mechanism limited by CO₂ adsorption or activation, analogous to behavior for unpromoted ceria catalysts.

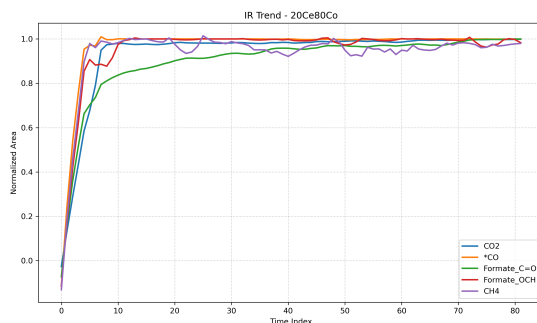


Figure 2.3: Normalized IR Intensities decay of 20Ce80Co.

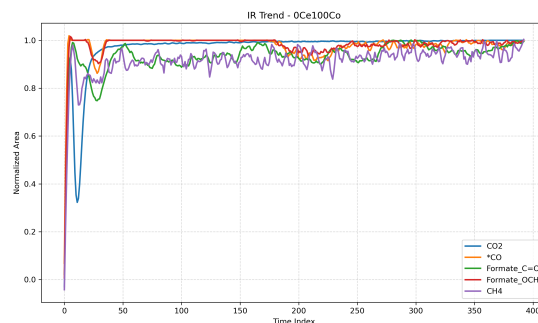


Figure 2.4: Normalized IR Intensities decay of 0Ce100Co.

2.6 | CO₂ methanation performance

As shown in Fig. A.15, the CO₂ conversion decreases at higher reduction temperatures (>300 °C), likely due to reduced surface hydrogen coverage that limits the hydrogenation of intermediates, consistent with observations on CoO–Co interfaces [13]. Additionally, the temperature of maximum conversion shifts from 200 °C for 0Ce100Co to 300 °C for Ce-containing catalysts, which may reflect a change in dominant reaction pathway—from a dissociative mechanism on cobalt to a carbon-formate mechanism promoted by ceria [14]. This is further supported by operando IR measurements at 200 °C, where 20Ce80Co shows high activity attributed to early activation of formate intermediates; however, confirmation at 300 °C would be valuable to correlate surface species with peak catalytic performance. The apparent activation energy (E_a) systematically decreases with increasing cerium content, from 94.18 kJ/mol for 0Ce100Co to 59.02 kJ/mol for 10Ce90Co, Fig. A.19. This trend likely reflects a shift in the dominant reaction mechanism, which requires less energy for CO₂ activation. Furthermore, the selectivity between catalysts at lower reduction temperatures is higher for 0Ce100Co. However, this selectivity quickly decreases at higher reduction temperatures of ≥ 250 °C, where Ceria catalysts have high selectivity of ≥ 94%, which confirms the different pathway mechanisms.

3 | Conclusion

This work highlights the potential of inverse CeO_x/Co catalysts for CO₂ methanation, demonstrating a possible structure-performance relationships supported by comprehensive characterization. Among the tested formulations, 20Ce80Co showed the highest CO₂ conversion and CH₄ space-time yield at 300 °C. At higher temperatures (>300 °C), reduced surface hydrogen coverage appears to limit methanation, underlining the importance of temperature control. The promotional role of ceria is evident: it enhances cobalt dispersion, lowers crystallinity (XRD), and increases oxygen mobility through Ce³⁺/Ce⁴⁺ redox cycling, thereby stabilizing active cobalt sites. H₂-TPR further confirms the formation of Co–O–Ce interfacial complexes that increase reduction temperatures and modify surface interactions. Operando IR spectroscopy reveals that different reaction mechanisms dominate across compositions, with formate and carbonyl intermediates playing key roles in Ce-containing catalysts. These mechanistic differences are critical to understanding and tuning catalytic activity. To fully capture these effects, further operando IR measurements at elevated temperatures (e.g., 300 °C) are recommended. Moreover, comparative studies with conventional Co/CeO_x systems under identical conditions are needed for a quantitative benchmark against the inverse architecture. Altogether, the inverse CeO_x/Co architecture enhances cobalt dispersion, alters mechanistic pathways, and improves catalytic performance. While it requires higher temperatures to reach its full potential, its behavior aligns with that of conventional Co/CeO_x systems, making it a promising candidate for Fischer–Tropsch-related chemistry and efficient low-temperature CO₂ methanation under optimized conditions.

4 | References

- [1] Asif Jan, Jisu Shin, Junsung Ahn, Sungeun Yang, Kyung Joong Yoon, Ji-Won Son, Hyoungchul Kim, Jong-Ho Lee, and Ho-Il Ji. Promotion of pt/ceo₂ catalyst by hydrogen treatment for low-temperature co oxidation. *RSC Adv.*, 9:27002–27012, 2019.
- [2] Sean S.-Y. Lin, Do Heui Kim, and Su Y. Ha. Metallic phases of cobalt-based catalysts in ethanol steam reforming: The effect of cerium oxide. *Applied Catalysis A: General*, 388(1-2):57–67, 2010.
- [3] Asif Jan, Jisu Shin, Junsung Ahn, Sungeun Yang, Kyung Joong Yoon, Ji-Won Son, Hyoungchul Kim, Jong-Ho Lee, and Ho-Il Ji. Promotion of pt/ceo₂ catalyst by hydrogen treatment for low-temperature co oxidation. *RSC Advances*, 9:27002–27012, 2019.
- [4] Timothy M. Roberge, Selasi O. Blavo, Chris Holt, Paul H. Matter, and John N. Kuhn. Effect of molybdenum on the sulfur-tolerance of cerium–cobalt mixed oxide water–gas shift catalysts. *Topics in Catalysis*, 56:1899–1906, 2013.
- [5] George E.P. O'Connell, Tze Hao Tan, Jodie A. Yuwono, Yu Wang, Amanj Kheradmand, Yijiao Jiang, Priyank V. Kumar, Rose Amal, Jason Scott, and Emma C. Lovell. Seeing the light: The role of cobalt in light-assisted co₂ methanation. *Applied Catalysis B: Environmental*, 343:123507, 2024.
- [6] Yuwen Zhou, Yuexiu Jiang, Zuzeng Qin, Qinruo Xie, and Hongbing Ji. Influence of zr, ce, and la on co₃o₄ catalyst for co₂ methanation at low temperature. *Chinese Journal of Chemical Engineering*, 2023. Available online.
- [7] Charles T. Campbell and Charles H. F. Peden. Oxygen vacancies and catalysis on ceria surfaces. *Science*, 309(5735):713, 2005.
- [8] Radu Craciun. Characterization of mixed amorphous/crystalline cerium oxide supported on sio₂data were collected at michigan state university, department of chemistry, usa.1. *Solid State Ionics*, 110(1):83–93, 1998.
- [9] G. Leendert Bezemer, Johannes H. Bitter, Herman P. C. E. Kuipers, Heiko Oosterbeek, Johannes E. Holewijn, Xiaoding Xu, Freek Kapteijn, A. Jos van Dillen, and Krijn P. de Jong. Cobalt particle size effects in the Fischer-tropsch reaction studied with carbon nanofiber supported catalysts. *Journal of the American Chemical Society*, 128(12):3956–3964, 2006. PMID: 16551103.
- [10] Jianqiang Wang, Meiqing Shen, Jun Wang, Jidong Gao, Jie Ma, and Shuangxi Liu. Ceo₂–coox mixed oxides: Structural characteristics and dynamic storage/release capacity. *Catalysis Today*, 175(1):65–71, 2011. The 6th International Conference on Environmental Catalysis (6th ICEC) Beijing, China, September 12-15, 2010.
- [11] Ijaz Hussain, Gazali Tanimu, Shakeel Ahmed, Chennampilly Ummer Aniz, Hassan Alasiri, and Khalid Alhooshani. A review of the indispensable role of oxygen vacancies for enhanced co₂ methanation activity over ceo₂-based catalysts: Uncovering, influencing, and tuning strategies. *International Journal of Hydrogen Energy*, 48(64):24663–24696, 2023. Catalytic Hydrogen Purification.
- [12] Job J. C. Struijs, Valery Muravev, Marcel A. Verheijen, Emiel J. M. Hensen, and Nikolay Kosinov. Ceria-supported cobalt catalyst for low-temperature methanation at low partial pressures of co₂. *Angewandte Chemie International Edition*, 62(5):e202214864, 2023.
- [13] Alexander Parastaev, Valery Muravev, Elisabet Huertas Osta, Tobias F. Kimpel, Jérôme F. M. Simons, Arno J. F. van Hoof, Evgeny Uslamin, Long Zhang, Job J. C. Struijs, Dudari B. Burueva, Ekaterina V. Pokochueva, Kirill V. Kovtunov, Igor V. Koptyug, Ignacio J. Villar-Garcia, Carlos Escudero, Thomas Altantzis, Pei Liu, Armand Béché, Sara Bals, Nikolay Kosinov, and Emiel J. M. Hensen. Breaking structure sensitivity in co₂ hydrogenation by tuning metal–oxide interfaces in supported cobalt nanoparticles. *Nature Catalysis*, 5(11):1051–1060, Nov 2022.
- [14] P.A. Ussa Aldana, F. Ocampo, K. Kobl, B. Louis, F. Thibault-Starzyk, M. Daturi, P. Bazin, S. Thomas, and A.C. Roger. Catalytic co₂ valorization into ch₄ on ni-based ceria-zirconia. reaction mechanism by operando ir spectroscopy. *Catalysis Today*, 215:201–207, 2013. Catalysis and synthetic fuels: state of the art and outlook.

A | Appendix A: Supportive Information

Operando Infrared (IR) Spectroscopy diagrams explanation

Figure A.1 illustrates the conditions employed during the operando infrared (IR) measurements for the two examined samples. Four distinct experimental conditions, labeled as (1) through (4), were applied during the analysis. These labels correspond directly to the spectral features observed in the IR spectra of each sample, enabling clear interpretation and comparison under varying conditions. Each condition represents a specific stage in the operando setup, allowing for a systematic evaluation of catalyst behavior during CO₂ methanation.

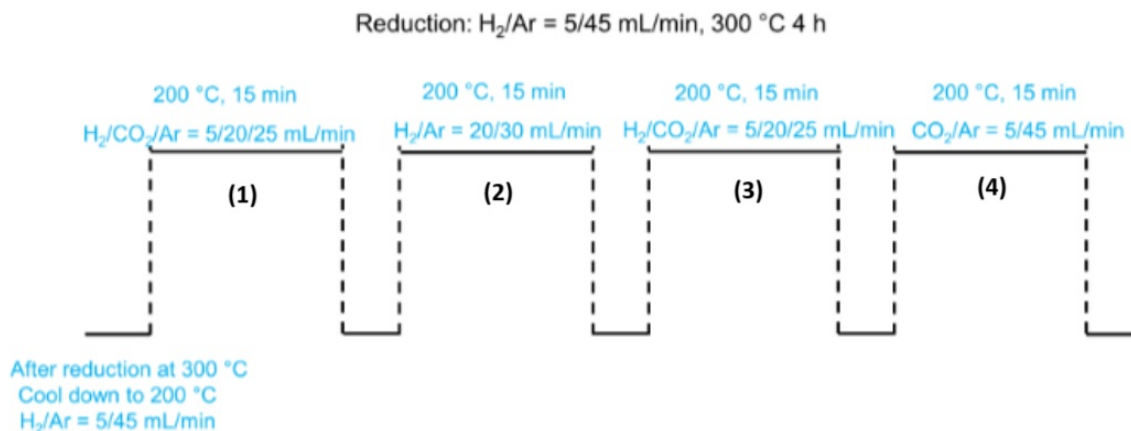


Figure A.1: IR:Conditions diagram of the experiment

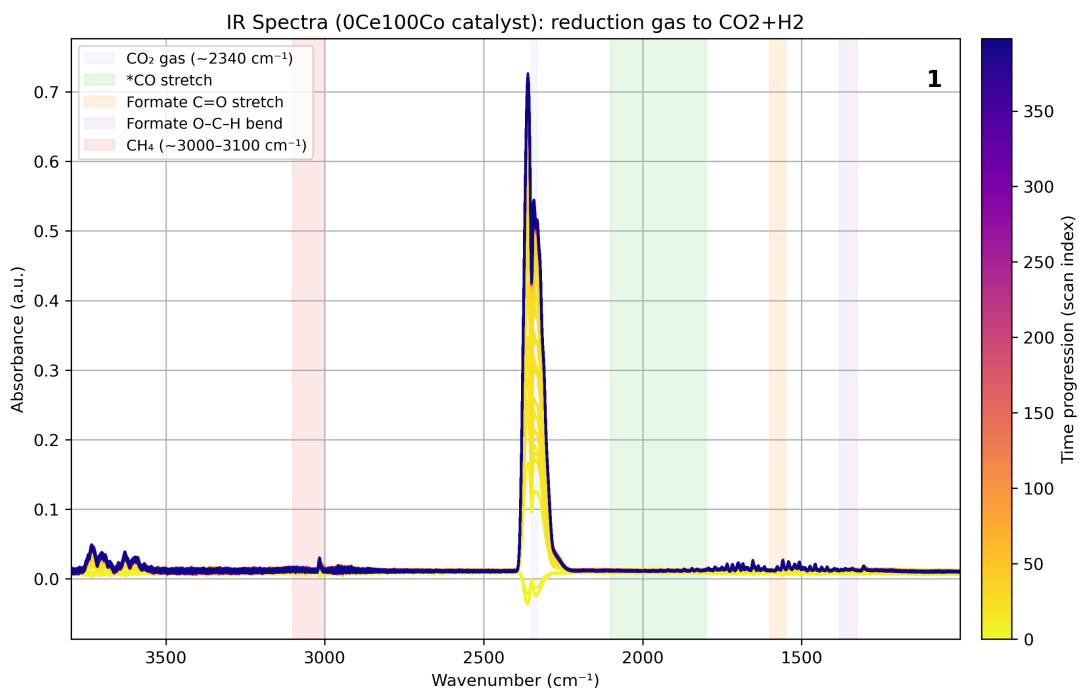


Figure A.2: CO₂ is introduced into the catalyst.

In the Fig. A.2 for the **0Ce100Co** catalyst, we introduce CO₂ + H₂ into the system and observe both CO₂ (at 2350 cm⁻¹) and CH₄ (in the 3000–3050 cm⁻¹ range) on the surface.

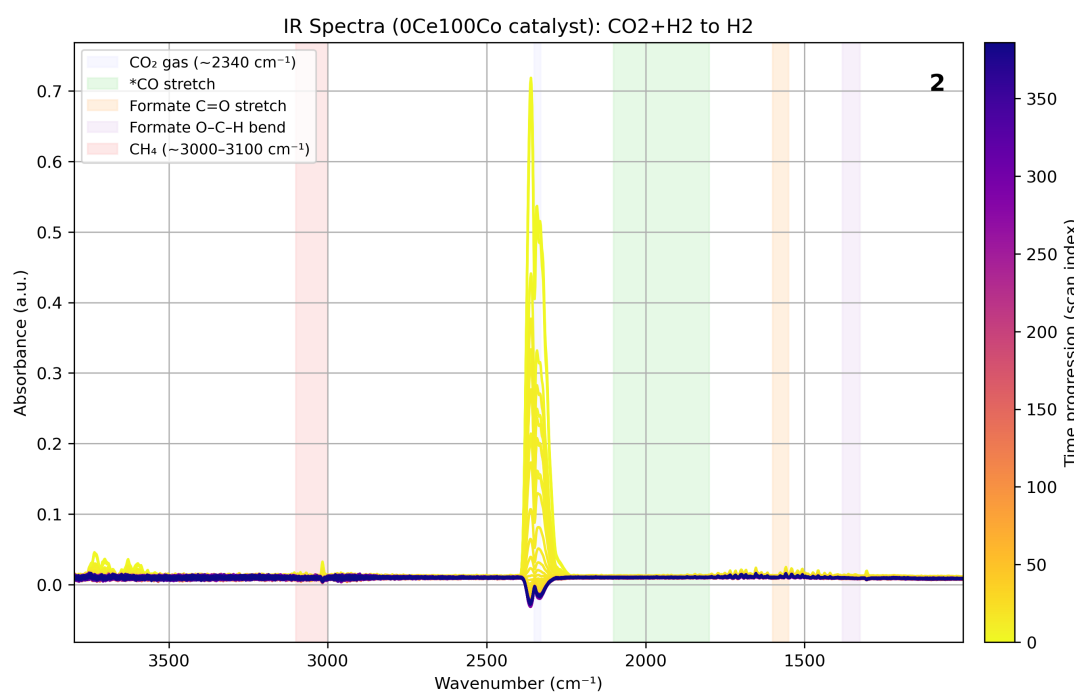


Figure A.3: CO₂ is removed, leaving only H₂

When CO₂ is removed and only H₂ is introduced, as shown in the Fig. A.3, there are no significant surface interactions observed.

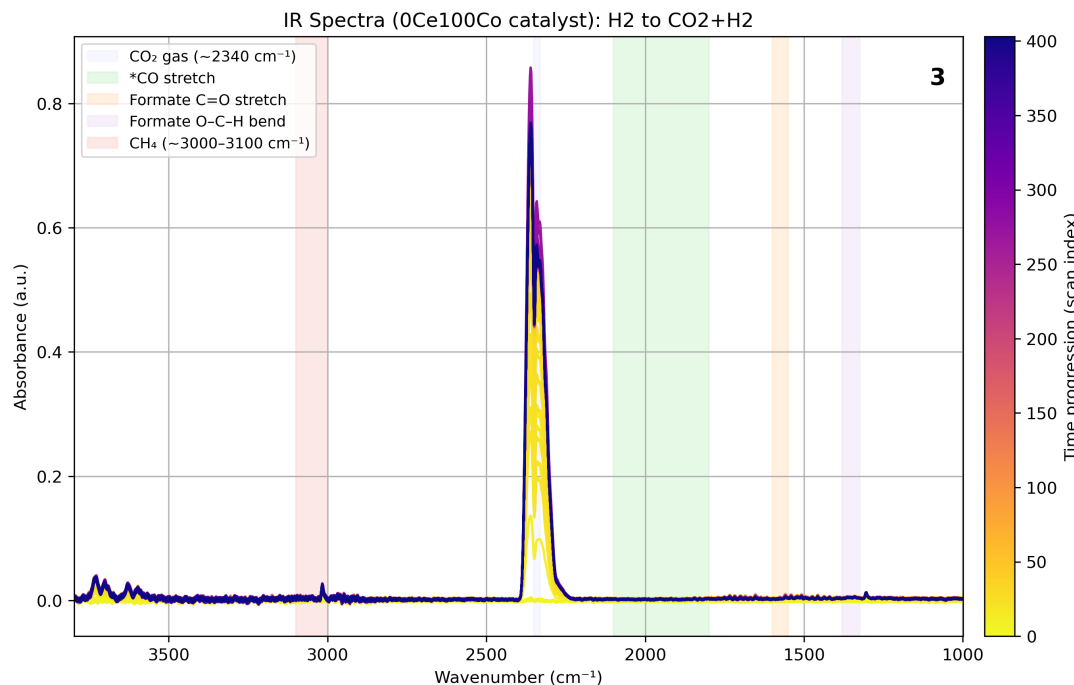


Figure A.4: CO₂ is reintroduced after a H₂-rich phase

In the Fig. A.4, under H₂-rich conditions, we reintroduce CO₂, and once again, both CO₂ (2350 cm⁻¹) and CH₄ (3000–3050 cm⁻¹) are observed on the surface.

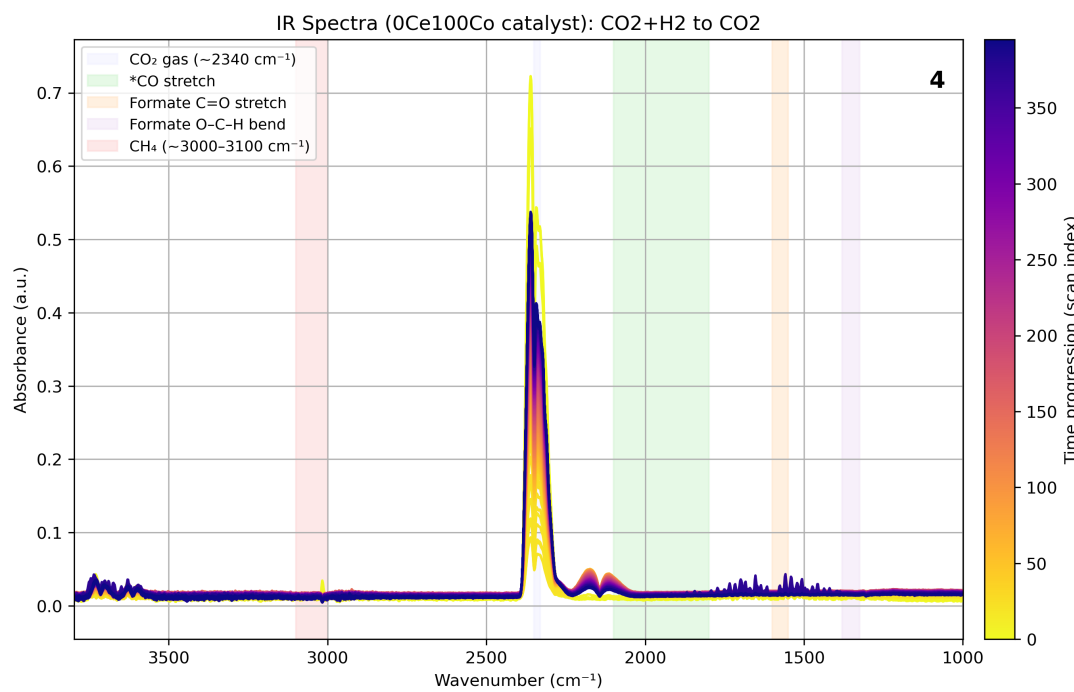


Figure A.5: H₂ is removed, only CO₂ remains

Finally, in the Fig. A.5, when H₂ is removed and only CO₂ remains, we observe a new absorption band in the 2000–2200 cm⁻¹ region, which suggests the possible formation or adsorption of CO on the surface. The band at 2358 cm⁻¹ was assigned to CO₂ asymmetric stretching vibration; bands at 2178 and 2110 cm⁻¹ were assigned to CO stretching modes.

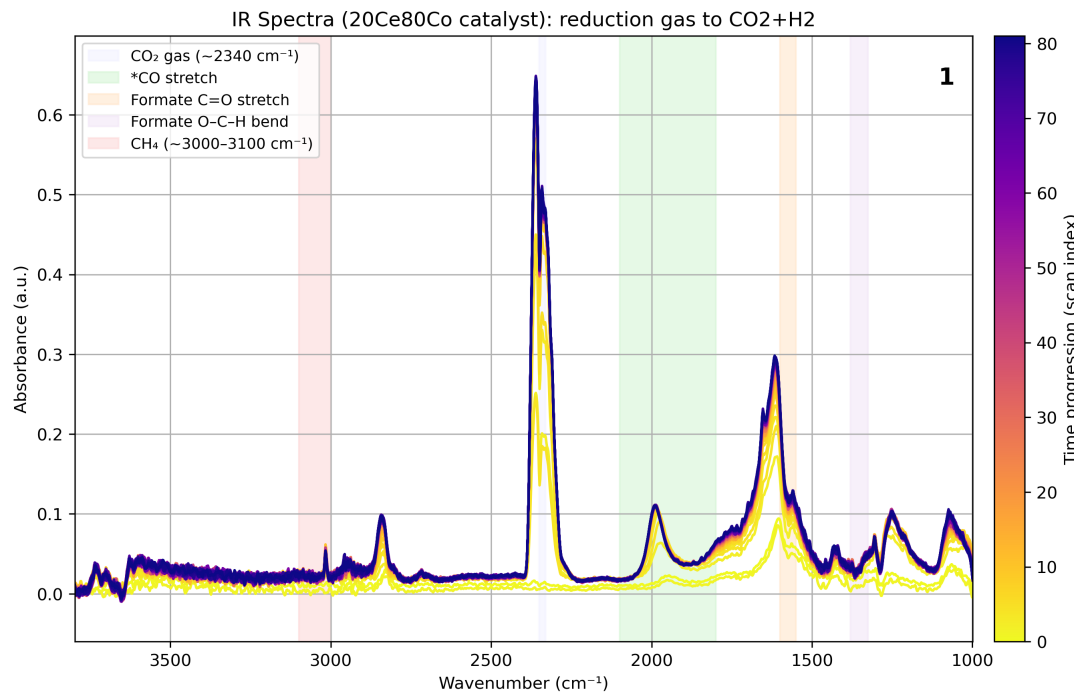


Figure A.6: CO₂ is introduced into the catalyst.

In the Fig. A.6 for the **20Ce80Co** catalyst, when CO₂ and H₂ are introduced, we observe multiple interactions on the surface. A strong band corresponding to gaseous CO₂ appears around 2340 cm⁻¹ (2330–2350 cm⁻¹). Additionally, we detect adsorbed CO, with a CO stretching band in the range of 1800–2100 cm⁻¹. The presence of formate species is indicated by characteristic C=O stretching vibrations between 1550–1650 cm⁻¹, and O-C-H bending modes in the region of 1325–1380 cm⁻¹. Finally, methane formation is evidenced by a band in the 3010–3020 cm⁻¹ range, corresponding to CH₄.

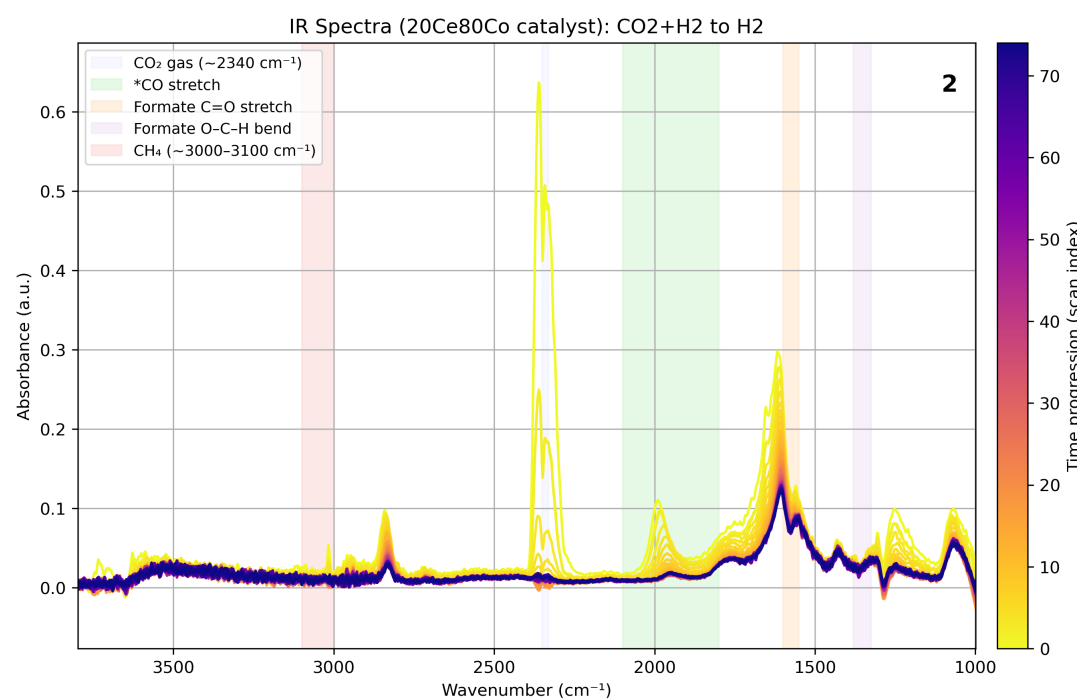


Figure A.7: CO₂ is removed, leaving only H₂

In the Fig. A.7, when CO₂ is removed and the system enters a high-H₂ phase, the intensity of the previously observed surface species decreases significantly. Notably, the CH₄ band (3010–3020 cm⁻¹) disappears, indicating that methane formation is closely linked to the presence of CO₂.

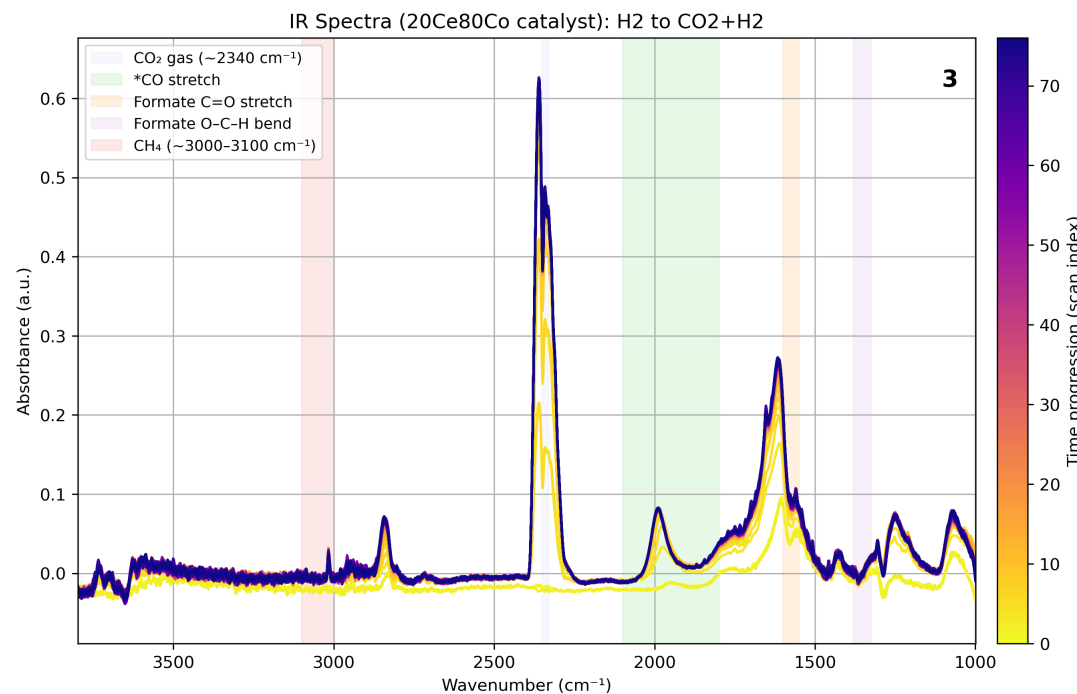


Figure A.8: CO₂ is reintroduced after a H₂-rich phase

In the Fig. A.8, when CO₂ is reintroduced under H₂-rich conditions, the same surface interactions observed in the first graph reappear—namely, the reformation of CH₄, CO, and formate species.

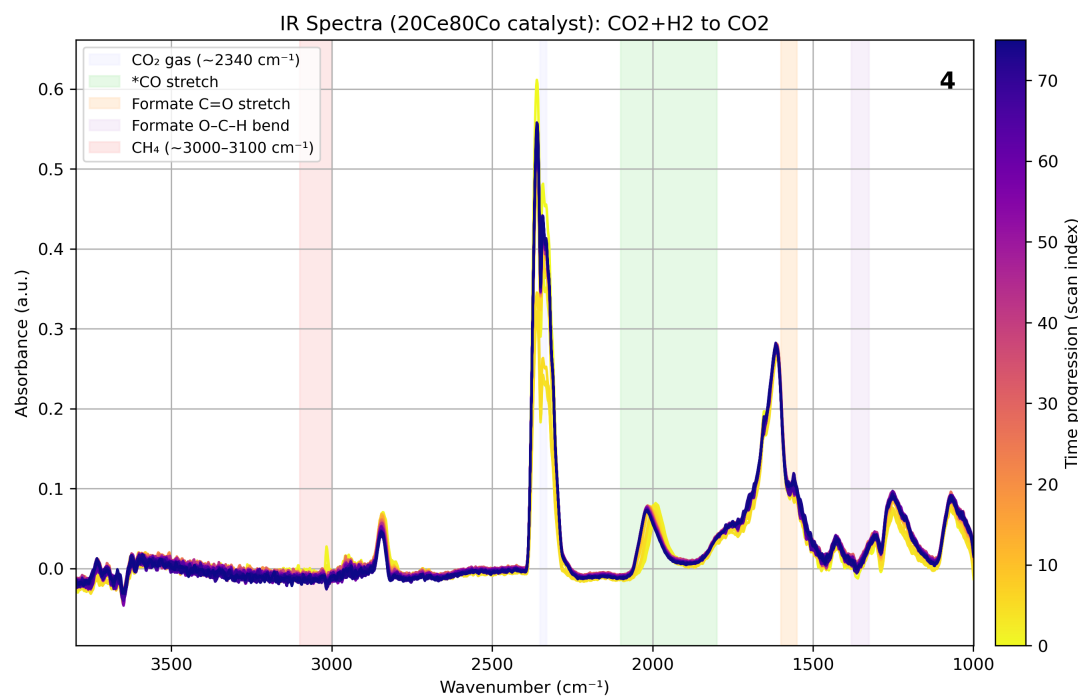


Figure A.9: H₂ is removed, only CO₂ remains

Finally, in the Fig. A.9, where only CO₂ is present without H₂, the surface still exhibits bands associated with adsorbed CO (1800–2100 cm⁻¹) and formate species (1550–1650 and 1325–1380 cm⁻¹), but the CH₄ signal is absent.

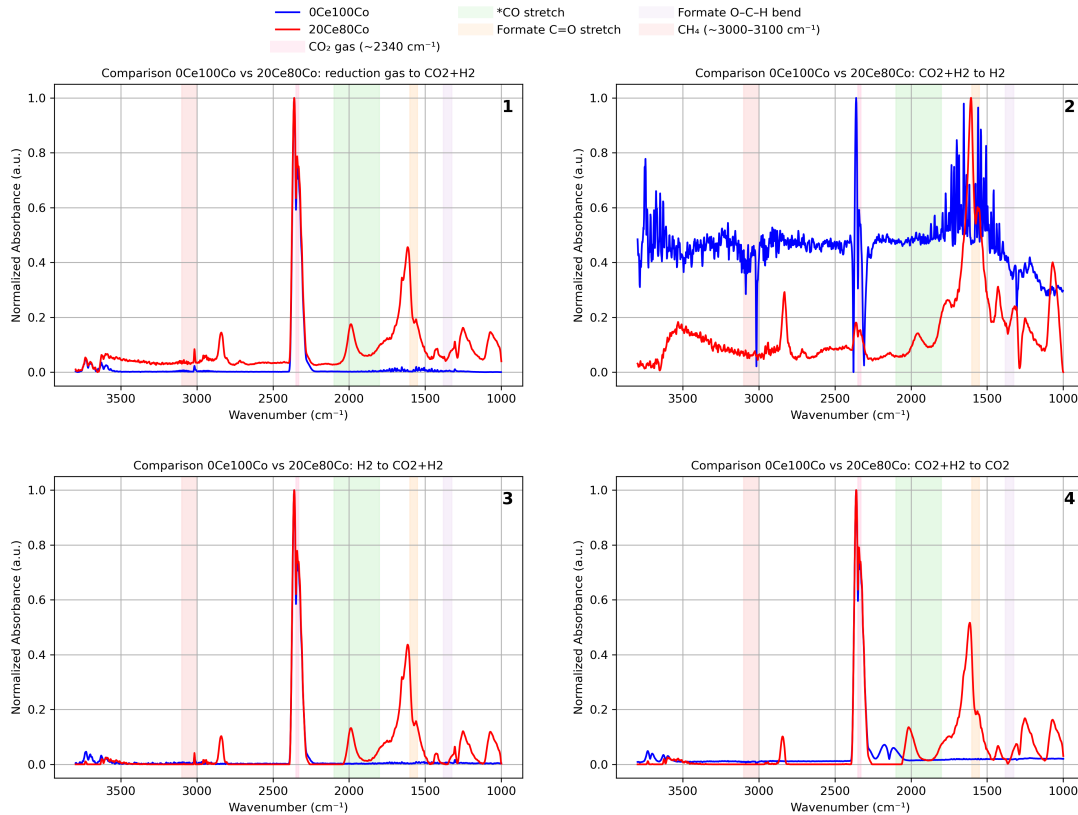


Figure A.10: Comparison of 0Ce100Co vs 20Ce80Co-Average Normalized Spectrum

We generated a set of normalized spectra, Fig. A.10, to enable a clearer comparison between **0Ce100Co** and **20Ce80Co** under each condition. These averaged, normalized plots are presented in the figure , where key vibrational bands are marked, allowing direct comparison of the surface interactions between the two catalysts.

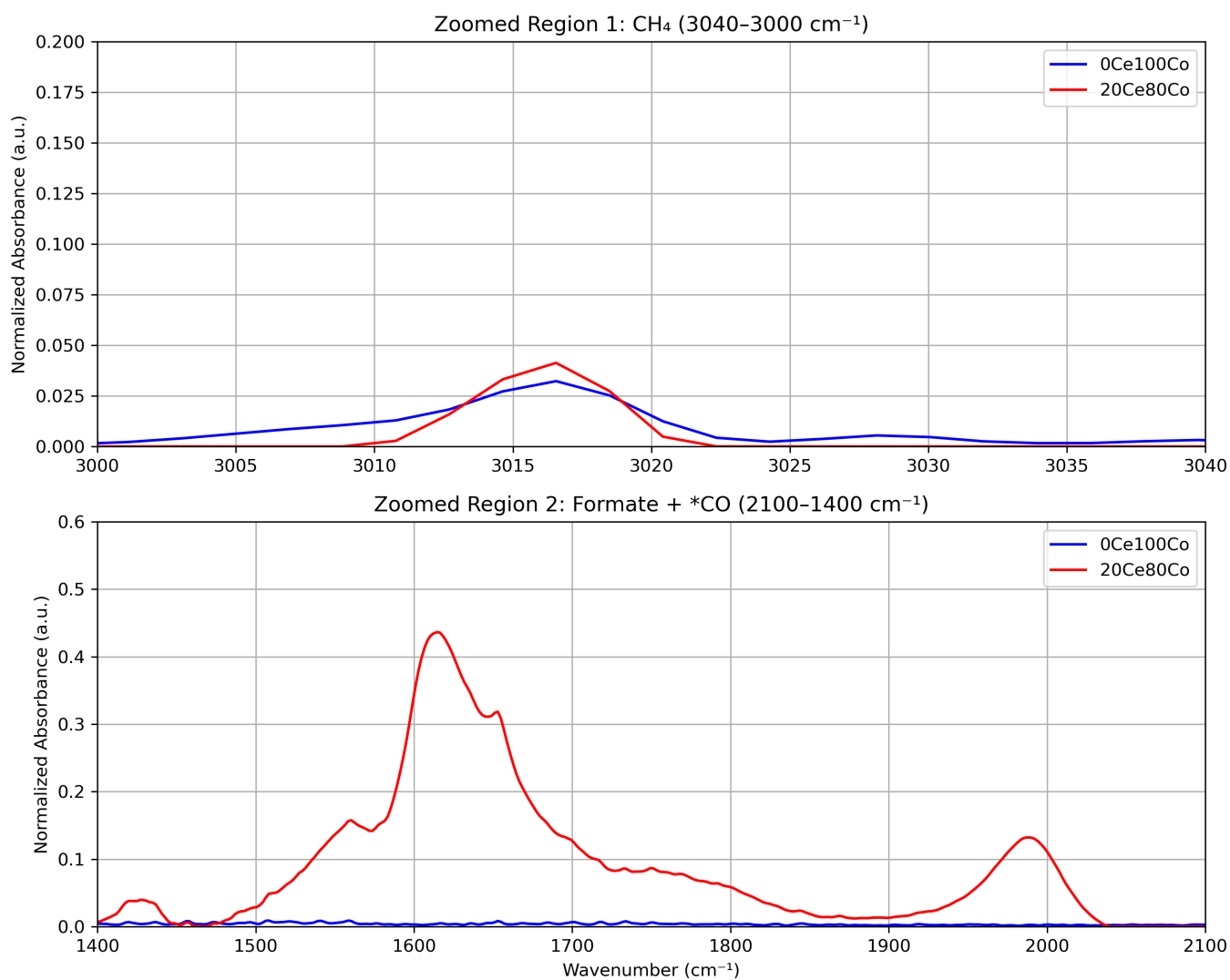


Figure A.11: Combined zoom of the comparison of 0Ce100Co vs 20Ce80Co-Average Normalized Spectrum from Methanation (3), Fig. A.4 and Fig. A.8

CO Chemisorption

Chemisorption measurements were performed to evaluate the cobalt dispersion on the catalyst surface. The table A.1 and Fig. A.12 summarizes the cobalt content, adsorption capacity, and calculated dispersion values for each sample.

wt.% Co	mmol Cobalt in 1 g sample	Co adsorption (mmol/g of sample)	Dispersion (%)
1.00	16.97	0.013	0.1%
0.97	16.57	0.04	0.2%
0.88	15.08	0.09	0.6%
0.79	13.42	0.13	1.0%
0.62	10.64	0.20	2.0%

Table A.1: Cobalt loading, adsorption, and dispersion data.

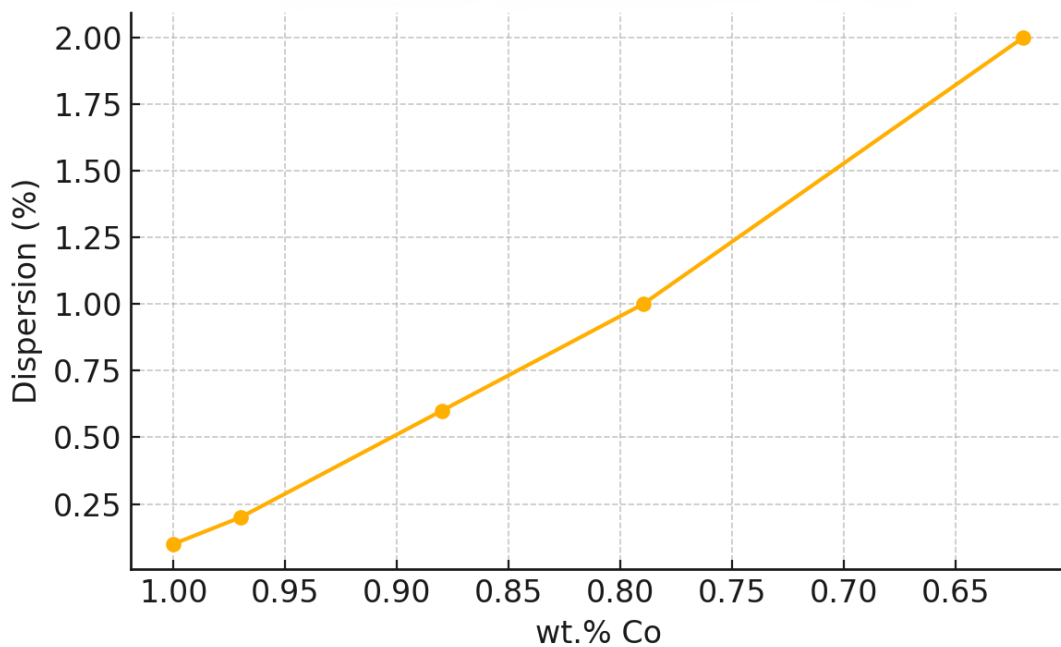


Figure A.12: Cobalt Dispersion Vs. Wt.% Co

X-Ray Diffraction (XRD)

X-ray diffraction (XRD) analysis was performed to identify the crystalline phases present in the catalysts and estimate the average crystallite size. Figure A.13 shows the XRD pattern, while Table A.2 summarizes the possible Miller indices corresponding to the observed diffraction peaks. The calculated particle sizes are presented in Table A.3. The possible presence of multiple crystalline phases, including CeO₂, Co₃O₄, CoO, Co, and Ce₂O₃, leads to significant peak overlap in the XRD diffractograms, complicating phase identification and quantitative analysis. While this limits the ability to draw definitive conclusions based on XRD alone, the data serve as a valuable tool for confirming hypotheses derived from complementary characterization techniques. A higher Ce concentration results in broader and less intense XRD peaks, indicating a lower degree of crystallinity. Increased crystallinity can enhance structural stability and lead to more well-defined active sites, which may improve catalyst durability. However, excessive crystallinity can also reduce the number of accessible active sites, limit structural flexibility, and potentially lower catalytic activity. Amorphous materials, on the other hand, tend to have more defects, unsaturated coordination sites, and potentially higher surface areas, which can enhance adsorption and reaction rates. In the diffraction pattern of 1Ce99Co a small peak can be seen at 23.6° which can be attributed to Ce₂O₃: Ce³⁺. This oxidation state is observed only in the sample with a very low cerium concentration and is further confirmed by the XANES analysis.

2θ (degree)	Possible Miller Indices				
	CeO ₂	Co ₃ O ₄	CoO	Co	Ce ₂ O ₃
23.6	-	100	-	-	100
28.7	111	-	-	-	100
31.3	200	220	-	-	-
36.7	-	311	111	101	-
44.9	-	400	-	111	112
47.6	220	-	-	-	-
55.9	311	422	-	-	-
59.5	222	511	220	-	-
65.2	-	440	-	-	-

Table A.2: Possible Miller Indices

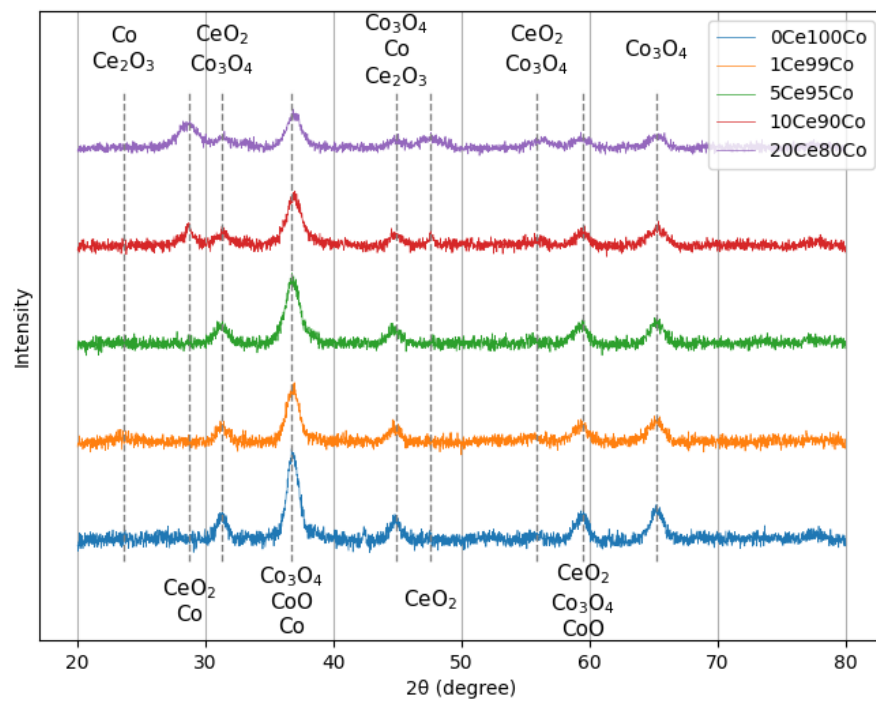


Figure A.13: XRD technique

XANES and Ce Oxidation States

Sample	Particle size (nm)
20Ce80Co	7.42
10Ce90Co	6.62
5Ce95Co	6.89
1Ce99Co	7.58
0Ce100Co	8.94

Table A.3: Particle sizes for different Cobalt calculated using XRD

X-ray Absorption Near Edge Structure (XANES) spectroscopy was employed to investigate the oxidation states of cerium in the catalyst samples. Figure A.14 presents the Ce L₃-edge spectra, including reference spectra for Ce³⁺ and Ce⁴⁺ (orange and blue dashed lines, respectively), alongside the samples of interest shown as solid lines. This analysis enables the assessment of the Ce³⁺/Ce⁴⁺ ratio in the prepared materials.

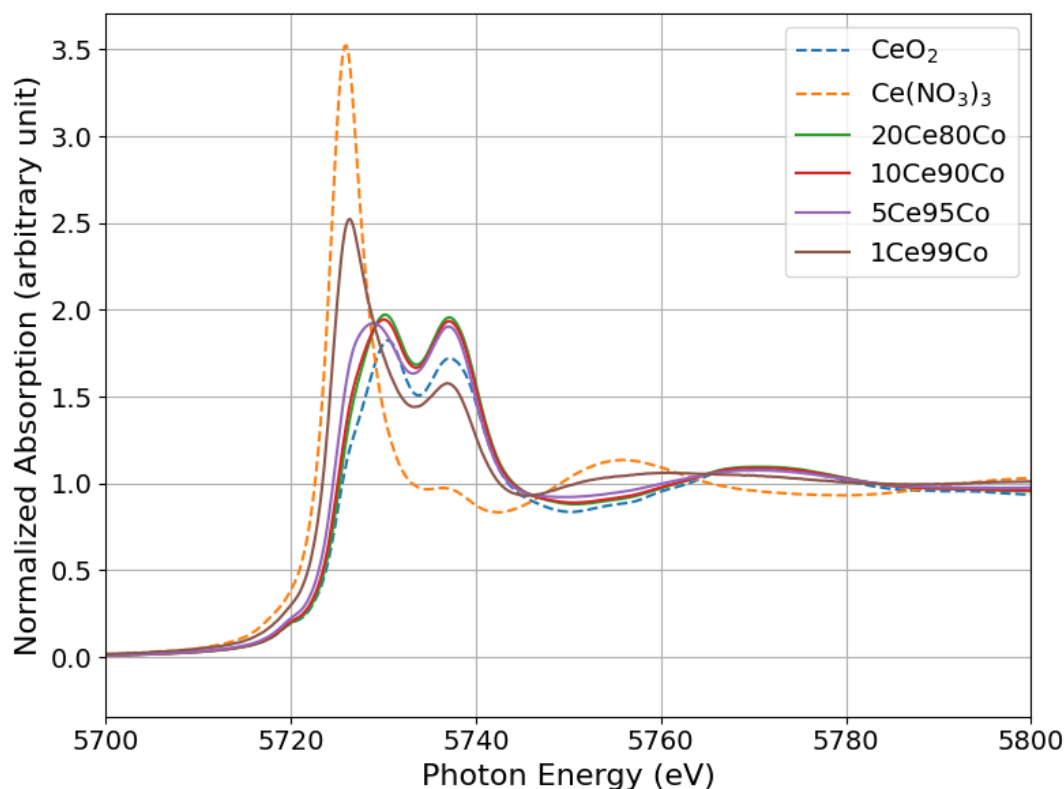


Figure A.14: XANES L₃ Edge for Ce³⁺ and Ce⁴⁺ reference (orange and blue dashed lines respectively) and the experimental samples in solid lines

CO₂ Hydrogenation Performance

The catalytic performance of the synthesized Ce-Co catalysts for CO₂ methanation was evaluated at different reduction temperatures, the measurement being carried out at a temperature of 200 °C with a feed gas of H₂/CO₂/He in a 12/2.5/37.5 mL/min flow ratio. Several key performance metrics were analyzed to assess the activity and selectivity of the materials.

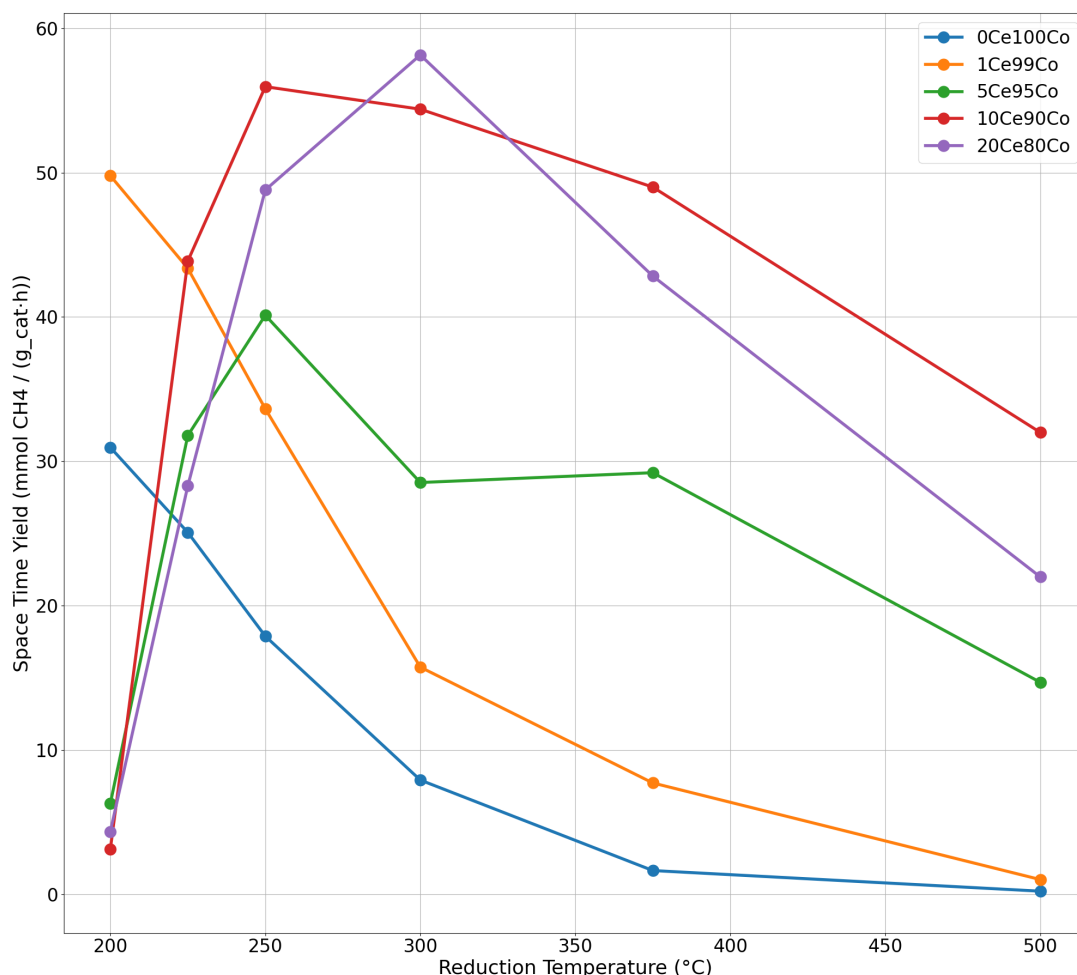


Figure A.15: Space time yield of CH₄ (mmol CH₄ / g_{cat} · h) as a function of reduction temperature.

Figure A.15 shows the space time yield of methane. A maximum activity is observed for the 10Ce90Co and 20Ce80Co samples, peaking around 275°C–300°C.

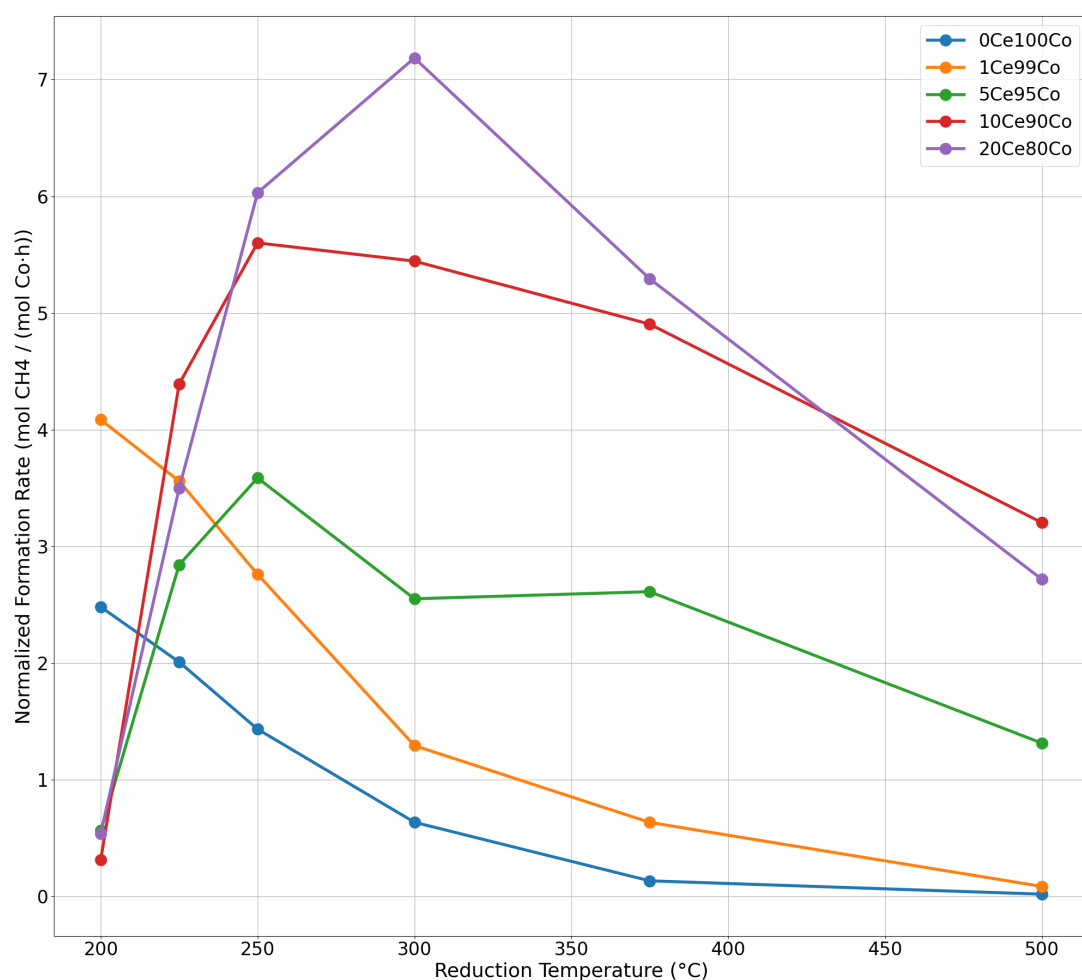


Figure A.16: Normalized CH₄ formation rate (mol CH₄ / mol Co · h) as a function of reduction temperature.

Figure A.16 presents the methane formation rate normalized to the cobalt content. The trend reveals improved intrinsic activity for Ce-containing samples, particularly 20Ce80Co.

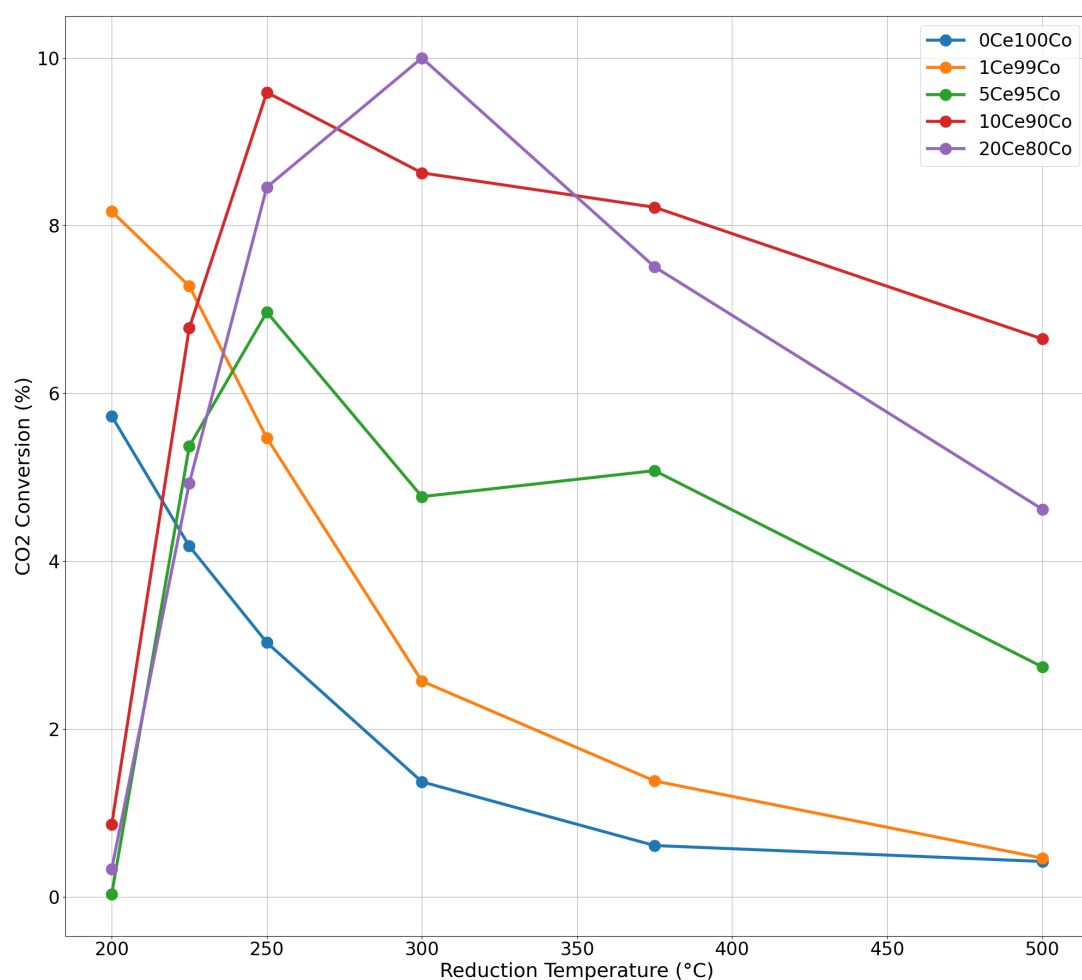


Figure A.17: CO₂ conversion (%) vs. reduction temperature.

As shown in Figure A.17, the CO₂ conversion exhibits a similar trend to the STY, with the 10Ce90Co and 20Ce80Co samples achieving the highest conversion values.

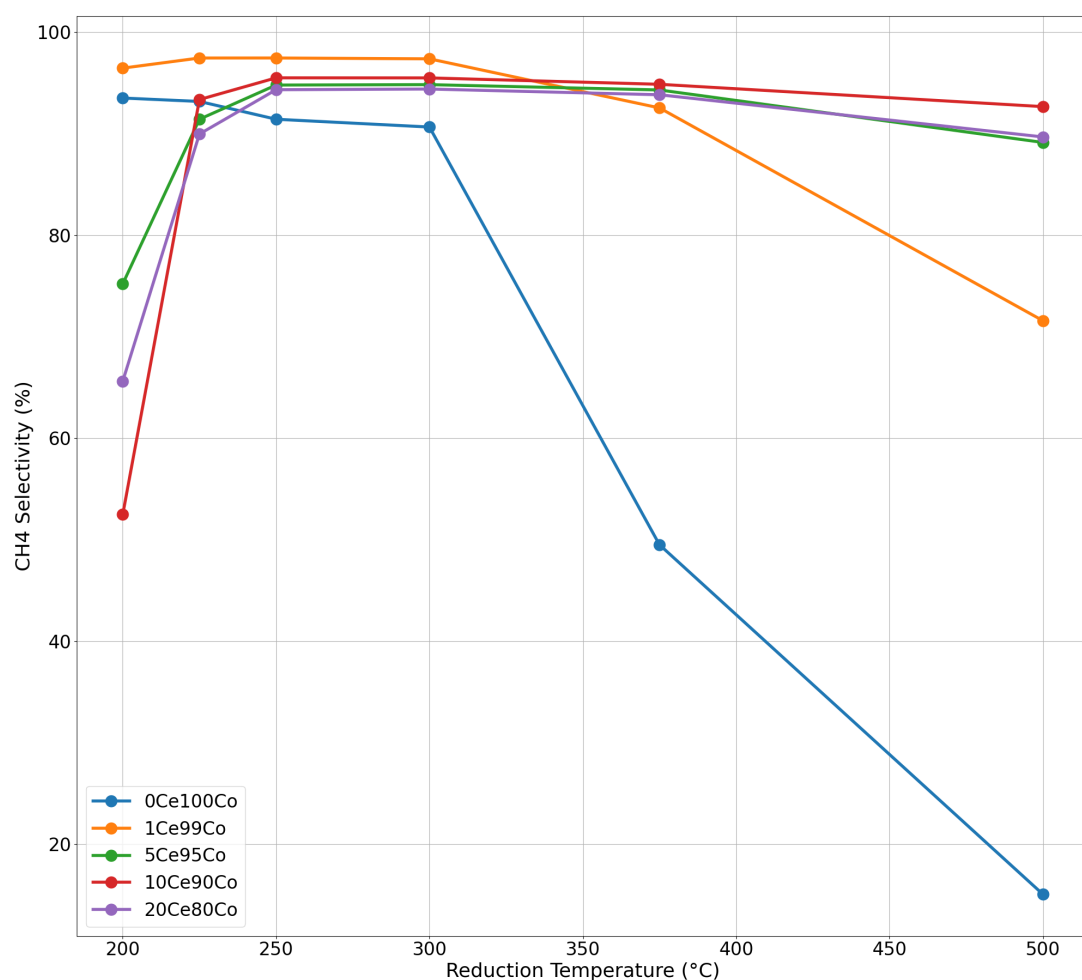


Figure A.18: CH₄ selectivity (%) vs. reduction temperature.

Figure A.18 shows that CH₄ selectivity remains high for all samples, although 0Ce100Co exhibits a noticeable drop at higher temperatures.

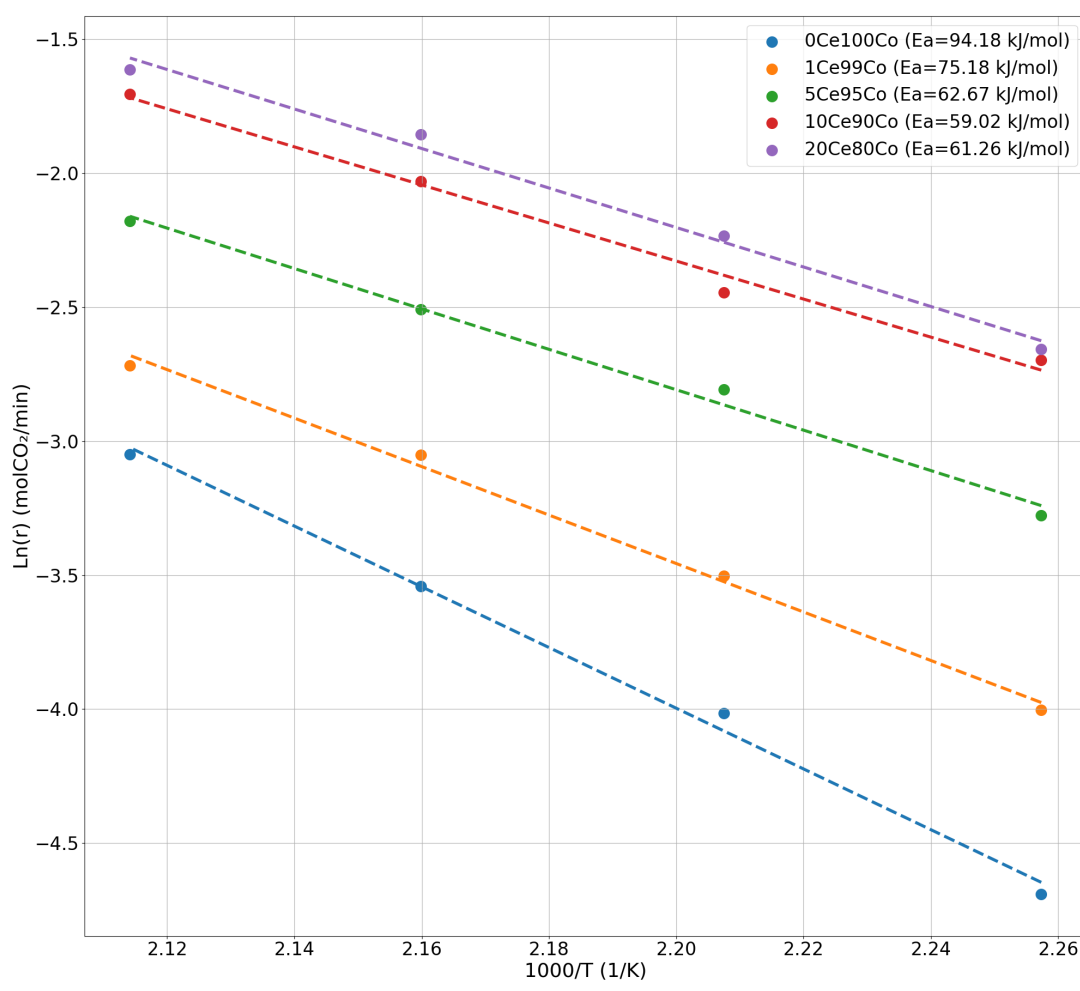


Figure A.19: Arrhenius plot used to determine the apparent activation energies (E_a) for CO₂ methanation.

The Arrhenius plot in Figure A.19 reveals decreasing activation energy with increasing cerium content, suggesting improved reducibility and catalytic efficiency in Ce-containing catalysts.